

# Experimental and Theoretical Revisit of Ca–H Superhydrides: Anharmonic Effects on Phase Stability and Superconductivity

Wenbo Zhao,<sup>1,2,†</sup> Qiushi Li,<sup>1,†</sup> Ying Sun,<sup>1,2,†</sup> Zefang Wang,<sup>1</sup> Hefei Li,<sup>1,3</sup>

Hanyu Liu,<sup>1,2,\*</sup> Hongbo Wang,<sup>3,‡</sup> Yu Xie,<sup>1,4,§</sup> and Yanming Ma<sup>1,3,5</sup>

<sup>1</sup>Key Laboratory of Material Simulation Methods and Software of Ministry of Education,  
College of Physics, Jilin University, Changchun 130012, China

<sup>2</sup>International Center of Future Science, Jilin University, Changchun 130012, China

<sup>3</sup>State Key Laboratory of Superhard Materials, College of Physics, Jilin University, Changchun 130012, China

<sup>4</sup>Key Laboratory of Physics and Technology for Advanced Batteries of Ministry of Education,  
College of Physics, Jilin University, Changchun 130012, China

<sup>5</sup>College of Physics, Zhejiang University, Hangzhou 310027, China

(Dated: December 4, 2025)

The prediction of superconductivity above 200 K in CaH<sub>6</sub> revolutionized research on hydrogen-rich superconductors, and subsequent experiments have verified this prediction, while unidentified peaks in XRD and the decrease in superconducting temperature upon decompression indicate that unresolved issues remain. In this work, we combine theory and experiment to construct an accurate temperature–pressure phase diagram of the Ca–H system and identify the stability ranges of the candidate superconducting phases by considering anharmonic effects. Our results demonstrate that type-I clathrate Ca<sub>8</sub>H<sub>46–δ</sub> structures become thermodynamically stable at 0 K when anharmonic effects are considered. Notably, we found that the previously predicted CaH<sub>6</sub> phase achieves stability above 500 K, underscoring the significant role of temperature and anharmonic effects in stabilizing this intriguing high-pressure phase. Experimentally, we have successfully synthesized Ca<sub>8</sub>H<sub>46–δ</sub> phases at low temperatures, thereby validating our theoretical predictions. Our findings offer insights into the structure and superconducting mechanisms of hydrides.

## 1. INTRODUCTION

High-temperature superconductivity has attracted great attention in the field of condensed matter physics[1–4]. Since Ashcroft proposed that metallic hydrides could serve as potential high-temperature superconductors in 2004, hydride-based systems has expanded rapidly[5]. Although early theoretical calculations predicted superconducting critical temperatures ( $T_c$ ) of up to  $\sim 100$  K in systems such as SiH, SnH, and PH, these predictions remained unverified experimentally[6–11]. It was not until 2012 that CaH<sub>6</sub> was predicted to exhibit superconductivity as high as 215 K under high pressure[12], reigniting interest in hydrogen-rich compounds, and subsequently guiding theoretical and experimental discoveries of record-breaking superconducting materials such as H<sub>3</sub>S, LaH<sub>10</sub>, and YH<sub>9</sub>[13–22], with the recent successful synthesis of the first room-temperature superconductor, LaSc<sub>2</sub>H<sub>24</sub>[23, 24], in particular, making hydrogen-rich superconductors a major focus of current superconductivity research.

However, the experimental realization of CaH<sub>6</sub> has not been straightforward. Early attempts at synthesis using H<sub>2</sub> as the hydrogen source produced only low-hydride phases[25, 26]. It was not until a decade later, with the introduction of ammonia borane (NH<sub>3</sub>BH<sub>3</sub>), that CaH<sub>6</sub> was successfully synthesized[27, 28]. X-ray diffraction (XRD) confirmed its structure to be consistent with theoretical predictions, and  $T_c$  as high as 215 K was observed. Yet, additional unidentified diffraction peaks

were also detected in the XRD patterns. Moreover, although theory predicts that the  $T_c$  should increase during decompression, the experiment instead shows that it stays nearly constant from 200 to 165 GPa and then decreases sharply below 165 GPa. These results suggest that the phase landscape of the Ca–H system may be more complex than previously anticipated.

Recently, more refined structural predictions have revealed a new cubic phase, Ca<sub>8</sub>H<sub>46</sub>[29, 30], which adopts the type-I clathrate structure initially synthesized in Ba<sub>8</sub>Si<sub>46</sub>[31]. With the inclusion of Ca<sub>8</sub>H<sub>46</sub> in the Ca–H phase diagram, this phase becomes thermodynamically stable, whereas CaH<sub>6</sub> becomes metastable. The calculated  $T_c$  is also close to the experimental results. Moreover, hydrogen vacancy structures (such as Ca<sub>8</sub>H<sub>45</sub> and Ca<sub>8</sub>H<sub>44</sub>) lead to structural distortions and a significant reduction in  $T_c$ , consistent with the experimentally observed trend of  $T_c$  suppression upon decompression. These observations imply that Ca<sub>8</sub>H<sub>46–δ</sub> may also be present among the synthesized phases. Therefore, determining the temperature–pressure stability ranges of these candidate superconducting phases is a great topic.

We employed machine learning potential based large-scale calculations to construct a temperature–pressure phase diagram of the Ca–H system that includes anharmonic effects, and identified the stability regions of potentially superconducting phases. Further experimental studies also discover the predicted structures Ca<sub>8</sub>H<sub>46–δ</sub> by tuning the laser heating temperature. The results show that Ca<sub>8</sub>H<sub>46–δ</sub> is thermodynamically stable at 0 K, while CaH<sub>6</sub> becomes stable at high temperatures

( $\sim 500$  K). A reduction in hydrogen content significantly suppresses superconductivity in both  $\text{CaH}_{6-\delta}$  and  $\text{Ca}_8\text{H}_{46-\delta}$ , which accounts for the observed decrease of  $T_c$  upon decompression. Guided by theoretical predictions, we successfully synthesized  $\text{Ca}_8\text{H}_{46-\delta}$  at 167 GPa under low-temperature conditions. This work not only clarifies the structural origin of superconductivity under different experimental conditions, but also highlights the critical role of lattice anharmonicity in hydrogen-rich superconductors. The established framework provides a consistent explanation for the experimental observations in the Ca–H system and offers theoretical guidance for the future design of stable high- $T_c$  hydride materials.

## 2. RESULTS

### Harmonic Temperature–Pressure Phase Diagram

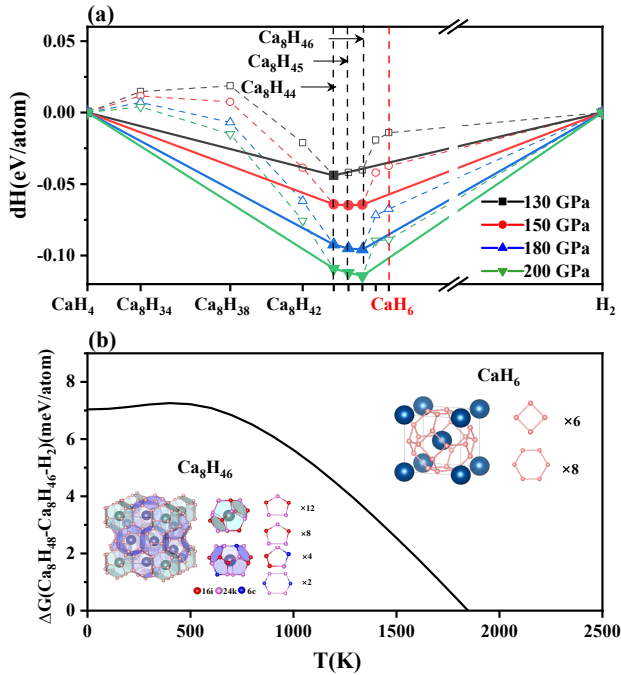


FIG. 1. (a) Formation enthalpy of Ca–H compounds at 130–200 GPa relative to  $\text{CaH}_4$  and  $\text{H}_2$ , calculated at the harmonic level. Solid symbols represent thermodynamically stable phases, while open symbols denote metastable ones. (b) Gibbs free energy difference between  $\text{Ca}_8\text{H}_{48}$  and  $\text{Ca}_8\text{H}_{46} + \text{H}_2$  as a function of temperature, calculated at the harmonic level.

To compute the temperature–pressure phase diagram of the Ca–H system, we first performed a comprehensive machine-learning accelerated structure search for  $\text{Ca}_8\text{H}_x$  ( $32 \leq x \leq 48$ ) at 130 GPa and constructed the 0 K harmonic phase diagram in the 130–200 GPa range. Consistent with previous findings[29, 30],  $\text{Ca}_8\text{H}_{44}$ ,  $\text{Ca}_8\text{H}_{45}$ ,

and  $\text{Ca}_8\text{H}_{46}$  become sequentially the most thermodynamically stable phases as pressure increases, culminating in the stabilization of  $\text{Ca}_8\text{H}_{46}$  above 180 GPa. In contrast,  $\text{CaH}_6$  remains metastable throughout, with an energy above the convex hull ( $E_{\text{hull}}$ ) of 20–26 meV/atom, which decreases with increasing pressure (Table S1).

Given hydrogen’s high vibrational frequencies, zero-point energy (ZPE) corrections are critical for accurately assessing hydride stability. To this end, phonon calculations were carried out for the candidate Ca–H structures. These calculations revealed that  $\text{Ca}_8\text{H}_{46}$  is dynamically stable only above 200 GPa, which is stricter than previously reported[29, 30], possibly due to the use of more stringent computational parameters (Supplementary Section 3).

Therefore, ZPE corrections were applied only at 200 GPa. At this pressure, the energy of  $\text{CaH}_6$  drops to just 7 meV/atom above the convex hull at 0 K. To further evaluate its finite-temperature stability, we calculated the Gibbs free energies, which show that  $\text{CaH}_6$  becomes thermodynamically stable at temperatures above roughly 1900 K. However, this estimate is based on solid  $\text{H}_2$  as the reference state, while  $\text{H}_2$  is liquid above 800 K at 200 GPa. Consequently, the actual stability temperature of  $\text{CaH}_6$  is likely even higher, and may exceed the experimental synthesis temperature ( $\sim 2000$  K). These findings highlight the limitations of harmonic approximations in explaining  $\text{CaH}_6$  formation under experimental conditions. To gain a more comprehensive understanding of phase stability and transition features in the Ca–H system, we further include anharmonic effects in our study.

### Anharmonic Temperature–Pressure Phase Diagram

We performed anharmonic free energy calculations on key structures  $\text{Ca}_8\text{H}_{44-48}$  from the harmonic phase diagram using our previously developed SS-CHA–ACNN method[32], which combines the stochastic self-consistent harmonic approximation (SSCHA)[33–35] with an attention-based neural network potential (ACNN)[36]. This approach significantly reduces computational cost, enabling anharmonic calculations for complex, multi-atom structures (see Supplementary Section 4 for details).

Including anharmonic effects has a noticeable impact on the predicted phase stability.  $\text{Ca}_8\text{H}_{44-46}$  all lie on the convex hull from 130 to 200 GPa, with  $\text{Ca}_8\text{H}_{46}$  consistently having the lowest enthalpy (Fig. 2). The dynamical stability of  $\text{Ca}_8\text{H}_{46}$  extends down to 130 GPa, well below the 200 GPa threshold predicted by harmonic calculations (Fig. S5). Meanwhile,  $\text{CaH}_6$ , though still slightly metastable, lies only 7–9 meV/atom above the hull, comparable to that obtained with harmonic ZPE (Table S1). Its thermodynamic stabilization temperature drops sharply to  $\sim 400$  K. These results indicate the for-

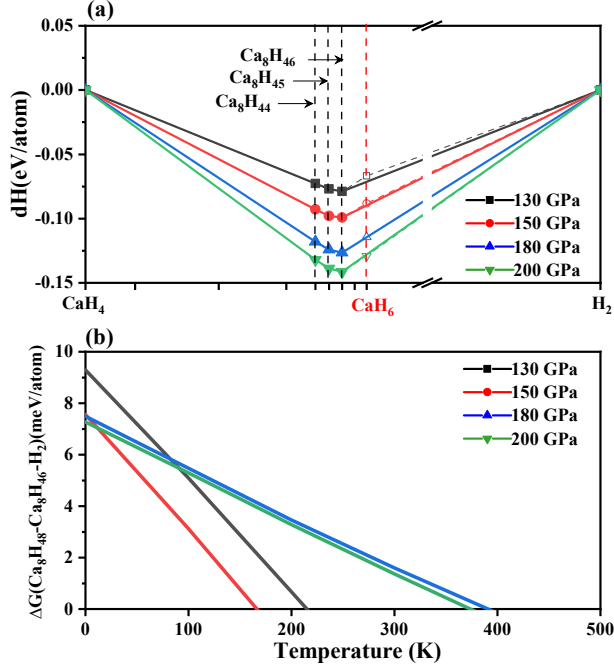


FIG. 2. (a) Formation enthalpy of Ca-H compounds at 130-200 GPa relative to  $\text{CaH}_4$  and  $\text{H}_2$ , calculated at the anharmonic level. Solid symbols represent thermodynamically stable phases, while open symbols denote metastable ones. (b) Gibbs free energy difference between  $\text{Ca}_8\text{H}_{48}$  and  $\text{Ca}_8\text{H}_{46} + \text{H}_2$  as a function of temperature, calculated at the anharmonic level.

mation of  $\text{CaH}_6$  under high-temperature synthesis conditions and suggest that  $\text{Ca}_8\text{H}_{46}$  is the stable feature at low temperatures. Motivated by this, we performed targeted synthesis experiments under different temperature conditions.

### Experiment

To investigate these predictions, we performed two high-pressure synthesis experiments using Ca and  $\text{BH}_3\text{NH}_3$  in laser-heated DACs at 165–167 GPa. The first sample was heated to approximately 2000 K under a pressure of about 166 GPa, and a superconducting transition was observed at around 215 K (Fig. S9), consistent with the reported superconducting transition temperature ( $T_c$ ) of  $\text{CaH}_6$ [28], thereby confirming its successful synthesis.

The second sample was then heated to a lower temperature under a similar pressure (164 GPa). Due to the weak blackbody radiation at this temperature, the emission spectrum could not be detected, and the heating temperature could not be estimated. Synchrotron XRD confirmed a cubic clathrate with a  $\text{Ca}_8\text{H}_{46}$ -type framework (Fig 3). The refined lattice parameter was

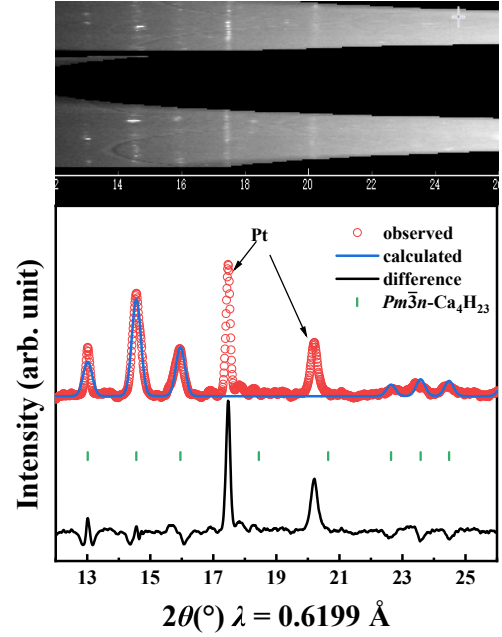


FIG. 3. Synchrotron XRD of  $\text{Ca}_8\text{H}_{46}$  collected at 167 GPa. The upper panel shows the 2D diffraction image (“cake”), while the lower panel presents the integrated diffraction pattern. Red circles are the observed XRD data, the blue line is the Rietveld refinement profile of  $\text{Ca}_8\text{H}_{46}$ , and the black line represents the difference between the observed and calculated intensities. Green ticks mark the Bragg peak positions of the  $\text{Pm}\bar{3}n\text{-Ca}_4\text{H}_{23}$  phase. Peaks labeled “Pt” originate from the platinum gasket.

$a = 5.447 \text{ \AA}$ , with a unit cell volume of  $161.61 \text{ \AA}^3$ . The unit cell volume is smaller than that of calculated  $\text{Ca}_8\text{H}_{46}$ . The EOS comparison shows it is close to  $\text{Ca}_8\text{H}_{44}$  (Fig. S10). Meanwhile, due to the nearly identical calculated XRD patterns of  $\text{Ca}_8\text{H}_{44-46}$  (Fig. S11), the synthesized phase is identified as a hydrogen-deficient  $\text{Ca}_8\text{H}_{46} - \delta$  composition. These results directly validate the phase stability trends predicted by our anharmonic calculations and support the revised superconducting phase diagram of the Ca-H system.

### Superconductivity

To further understand superconducting behavior, we examined the structural and electronic properties of  $\text{Ca}_8\text{H}_{42-48}$  compositions. Structure predictions reveal that most compositions within this range can stabilize in two distinct hydrogen cages,  $\text{CaH}_6$ -type and  $\text{Ca}_8\text{H}_{46}$ -type, denoted as  $\text{CaH}_{6-\delta}$  and  $\text{Ca}_8\text{H}_{46-\delta}$ , respectively. The only exception is  $\text{Ca}_8\text{H}_{48}$  ( $\text{CaH}_6$ ), where excess hydrogen suppresses formation of the  $\text{Ca}_8\text{H}_{46}$ -type clathrate structure, and can only stabilize the  $\text{CaH}_6$ -

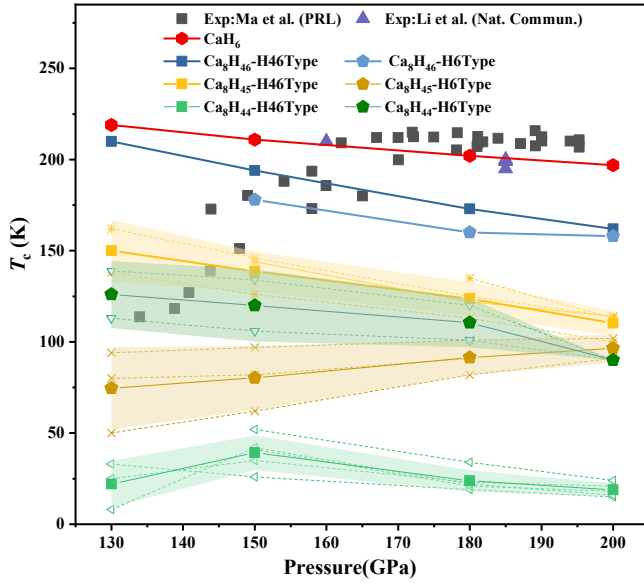


FIG. 4. Pressure dependence of  $T_c$  in Ca-H Superhydrides. The figure presents calculated anharmonic  $T_c$  for  $\text{CaH}_6$  and  $\text{Ca}_8\text{H}_{44-46}$  in two structural types:  $\text{Ca}_8\text{H}_{46-\delta}$  and  $\text{CaH}_{6-\delta}$ . For each type, multiple space group structures were considered. Hollow symbols and dashed lines represent individual calculations, while solid symbols and solid lines indicate their averages. Shaded regions denote the estimated error range. Experimental data from Ma *et al.* [28] and Li *et al.* [27] are shown as black squares and a purple triangle, respectively.

type cage. All compositions favor the  $\text{Ca}_8\text{H}_{46}$ -type cage energetically, except for  $\text{Ca}_8\text{H}_{48}(\text{CaH}_6)$  (Table S4). Notably, as the hydrogen content increases, the energy of the  $\text{CaH}_6$ -type framework gradually decreases, narrowing the energetic gap between the two distinct hydrogen cages.

We selected representative low-enthalpy structures derived from these two cage types and systematically analyzed their electronic density of states (see Supplementary Section 6). The results show that while cage geometry and structural symmetry affect the electronic structure, stoichiometry plays the dominant role. As hydrogen content decreases, the density of states at the Fermi level ( $N(E_F)$ ) gradually drops for both  $\text{CaH}_{6-\delta}$  and  $\text{Ca}_8\text{H}_{46-\delta}$  (Fig. S8). Some structures of  $\text{Ca}_8\text{H}_{44}$  may even become insulating and require compression to regain metallicity under low pressure. Notably,  $\text{Ca}_8\text{H}_{48}(\text{CaH}_6)$  shows a lower  $N(E_F)$  than  $\text{Ca}_8\text{H}_{46}$  despite having more hydrogen, while the fully occupied  $\text{Pm}\bar{3}\text{n}-\text{Ca}_8\text{H}_{46}$  structure exhibits the highest  $N(E_F)$  (Fig. S8).

Due to computational limitations, anharmonic superconductivity calculations were performed only for the stable phases at each composition (Table S8). The results show a consistent trend across compositions: structural

symmetry remains unchanged, lattice volume slightly expands, the frequency range of hydrogen-related optical phonons becomes significantly compressed, and some phonon modes that strongly contribute to electron-phonon coupling (EPC) are weakened, leading to a consequent decrease in the  $T_c$  (Fig. S15-S16).

Guided by this trend, we performed harmonic calculations on representative  $\text{Ca}_8\text{H}_{46-\delta}$  and  $\text{CaH}_{6-\delta}$  cages and applied scaling corrections to estimate  $T_c$  (see Supplementary Section 7 for details). The results show that  $\text{CaH}_6$  exhibits the highest predicted  $T_c$ , closely matching experimental observations under high-temperature and high-pressure synthesis (Fig. 4). The  $T_c$  of  $\text{Pm}\bar{3}\text{n}-\text{Ca}_8\text{H}_{46}$  is lower than that of  $\text{CaH}_6$ , with the difference increasing to approximately 30 K as pressure increases, which differs from previous reports at harmonic level[30]. The convergence tests of superconducting parameters are shown in Supplementary Material 3.  $\text{Ca}_8\text{H}_{46}$  with a  $\text{CaH}_6$ -type clathrate structure exhibits an even lower  $T_c$ . The deviation from the trend observed in  $N(E_F)$  may be attributed to the high phonon frequencies and strong electron-phonon coupling in  $\text{CaH}_6$ , further supporting it as the origin of the high- $T_c$  superconducting phase reported in earlier experiments.

Meanwhile, a consistent trend:  $\text{CaH}_6 > \text{Ca}_8\text{H}_{46} > \text{Ca}_8\text{H}_{45} > \text{Ca}_8\text{H}_{44}$ , is observed in both  $\text{Ca}_8\text{H}_{46-\delta}$  and  $\text{CaH}_{6-\delta}$  cages, at both harmonic and anharmonic levels. This progression explains the rapid suppression of superconductivity observed experimentally upon decompression.

### 3. DISCUSSION

Our work clarifies the stability ranges of all potentially superconducting phases in the Ca-H system across pressure and temperature. We identify  $\text{Ca}_8\text{H}_{46-\delta}$  as the thermodynamically stable phase at low temperatures, while  $\text{CaH}_{6-\delta}$  becomes accessible at high temperatures ( $\sim 500$  K). The observed decrease in  $T_c$  upon decompression is primarily attributed to a reduction in hydrogen content. Guided by theory, we successfully synthesized high- $T_c$   $\text{CaH}_6$  under high-pressure and high-temperature conditions by tuning the laser heating temperature, and obtained low- $T_c$   $\text{Ca}_8\text{H}_{46-\delta}$  at lower temperatures. Our findings clearly explain the experimentally observed emergence of high- $T_c$  and low- $T_c$  phases and their temperature and pressure dependence. Moreover, highlight the critical role of temperature and anharmonic effects in stabilizing high-pressure superconducting phases.



## REFERENCES

- 
- <sup>†</sup> These three authors contributed equally  
<sup>\*</sup> hanyuliu@jlu.edu.cn  
<sup>‡</sup> whb2477@jlu.edu.cn  
<sup>§</sup> xieyu@jlu.edu.cn
- [1] Y. Sun, X. Zhong, H. Liu, and Y. Ma, *National Science Review* **11**, nwad270 (2024).
  - [2] X. Zhang, Y. Zhao, F. Li, and G. Yang, *Matter and Radiation at Extremes* **6**, 10.1063/5.0065287 (2021).
  - [3] M. Du, W. Zhao, T. Cui, and D. Duan, *Journal of Physics: Condensed Matter* **34**, 173001 (2022).
  - [4] B. Lilia, R. Hennig, P. Hirschfeld, G. Profeta, A. Sanna, E. Zurek, W. E. Pickett, M. Amsler, R. Dias, M. I. Eremets, *et al.*, *Journal of Physics: Condensed Matter* **34**, 183002 (2022).
  - [5] N. W. Ashcroft, *Phys. Rev. Lett.* **92**, 187002 (2004).
  - [6] M. I. Eremets, I. A. Trojan, S. A. Medvedev, J. S. Tse, and Y. Yao, *Science* **319**, 1506 (2008).
  - [7] Y. Yao, J. S. Tse, Y. Ma, and K. Tanaka, *Europhysics Letters* **78**, 37003 (2007).
  - [8] Y. Li, G. Gao, Y. Xie, Y. Ma, T. Cui, and G. Zou, *Proceedings of the National Academy of Sciences* **107**, 15708 (2010).
  - [9] J. S. Tse, Y. Yao, and K. Tanaka, *Physical Review Letters* **98**, 117004 (2007).
  - [10] A. P. Drozdov, M. I. Eremets, and I. A. Trojan, arXiv (2015), arXiv:1508.06224 [cond-mat.supr-con].
  - [11] H. Liu, Y. Li, G. Gao, J. S. Tse, and I. I. Naumov, *The Journal of Physical Chemistry C* **120**, 3458 (2016), doi: 10.1021/acs.jpcc.5b12009.
  - [12] H. Wang, J. S. Tse, K. Tanaka, T. Iitaka, and Y. Ma, *Proceedings of the National Academy of Sciences* **109**, 6463 (2012).
  - [13] A. P. Drozdov, M. I. Eremets, I. A. Trojan, V. Ksenofontov, and S. I. Shylin, *Nature* **525**, 73 (2015).
  - [14] D. Duan, Y. Liu, F. Tian, D. Li, X. Huang, Z. Zhao, H. Yu, B. Liu, W. Tian, and T. Cui, *Scientific Reports* **4**, 6968 (2014).
  - [15] Y. Li, J. Hao, H. Liu, Y. Li, and Y. Ma, *J Chem Phys* **140**, 174712 (2014).
  - [16] M. Somayazulu, M. Ahart, A. K. Mishra, Z. M. Geballe, M. Baldini, Y. Meng, V. V. Struzhkin, and R. J. Hemley, *Phys. Rev. Lett.* **122**, 027001 (2019).
  - [17] A. P. Drozdov, P. P. Kong, V. S. Minkov, S. P. Besedin, M. A. Kuzovnikov, S. Mozaffari, L. Balicas, F. F. Balakirev, D. E. Graf, V. B. Prakapenka, E. Greenberg, D. A. Knyazev, M. Tkacz, and M. I. Eremets, *Nature* **569**, 528 (2019).
  - [18] F. Hong, L. Yang, P. Shan, P. Yang, Z. Liu, J. Sun, Y. Yin, X. Yu, J. Cheng, and Z. Zhao, *Chinese Physics Letters* **37**, 107401 (2020).
  - [19] Y. Ge, F. Zhang, and R. J. Hemley, *Physical Review B* **104**, 214505 (2021).
  - [20] D. V. Semenok, I. A. Kruglov, D. Zhou, D. Duan, A. R. Oganov, *et al.*, *Advanced Materials* **34**, 2204038 (2022).
  - [21] I. A. Troyan, D. V. Semenok, A. G. Kvashnin, A. V. Sadakov, O. A. Sobolevskiy, V. M. Pudalov, A. G. Ivanova, V. B. Prakapenka, E. Greenberg, A. G. Gavriliuk, I. S. Lyubutin, V. V. Struzhkin, A. Bergara, I. Errea, R. Bianco, M. Calandra, F. Mauri, L. Monacelli, R. Akashi, and A. R. Oganov, *Advanced Materials* **33**, 2006832 (2021).
  - [22] P. Kong, V. S. Minkov, M. A. Kuzovnikov, A. P. Drozdov, S. P. Besedin, S. Mozaffari, L. Balicas, F. F. Balakirev, V. B. Prakapenka, S. Chariton, D. A. Knyazev, E. Greenberg, and M. I. Eremets, *Nature Communications* **12**, 5075 (2021).
  - [23] X.-L. He, W. Zhao, Y. Xie, A. Hermann, R. J. Hemley, H. Liu, and Y. Ma, *Proceedings of the National Academy of Sciences* **121**, e2401840121 (2024).
  - [24] Y. Song, C. Ma, H. Wang, M. Zhou, Y. Qi, W. Cao, S. Li, H. Liu, G. Liu, and Y. Ma, *Room-temperature superconductivity at 298 K in ternary la-sc-h system at high-pressure conditions* (2025), arXiv:2510.01273 [cond-mat.supr-con].
  - [25] H. Fujihisa, Y. Nakamoto, M. Sakata, K. Shimizu, T. Matsuoka, Y. Ohishi, H. Yamawaki, S. Takeya, and Y. Gotoh, *Phys. Rev. Lett.* **110**, 235501 (2013).
  - [26] G. Wu, X. Huang, H. Xie, X. Li, M. Liu, Y. Liang, Y. Huang, D. Duan, F. Li, B. Liu, and T. Cui, *The Journal of Chemical Physics* **150**, 044507 (2019).
  - [27] Z. Li, X. He, C. Zhang, X. Wang, S. Zhang, Y. Jia, S. Feng, K. Lu, J. Zhao, and J. Zhang, *Nature communications* **13**, 2863 (2022).
  - [28] L. Ma, K. Wang, Y. Xie, X. Yang, Y. Wang, M. Zhou, H. Liu, X. Yu, Y. Zhao, and H. Wang, *Physical Review Letters* **128**, 167001 (2022).
  - [29] Y. Sun, A. Ellis, X. Chen, and M. Miao, *Journal of the American Chemical Society* **147**, 40407 (2025), pMID: 41123128.
  - [30] D. An, D. Duan, Z. Zhang, Q. Jiang, T. Ma, Z. Huo, H. Song, and T. Cui, *Phys. Rev. B* **110**, 054505 (2024).
  - [31] S. Yamanaka, E. Enishi, H. Fukuoka, and M. Yasukawa, *Inorganic Chemistry* **39**, 56 (2000), pMID: 11229033.
  - [32] W. Zhao, Y. Sun, J. Li, P. Yuan, T. Iitaka, X. Zhong, H. Li, Y.-W. Fang, H. Liu, I. Errea, and Y. Xie, *npj Computational Materials* **11**, 347 (2025).
  - [33] I. Errea, M. Calandra, and F. Mauri, *Phys. Rev. Lett.* **111**, 177002 (2013).
  - [34] R. Bianco, I. Errea, L. Paulatto, M. Calandra, and F. Mauri, *Phys. Rev. B* **96**, 014111 (2017).
  - [35] L. Monacelli, I. Errea, M. Calandra, and F. Mauri, *Phys. Rev. B* **98**, 024106 (2018).
  - [36] J. Li, J. Feng, J. Luo, B. Jiang, X. Zheng, Q. Song, J. Lv, K. Butler, H. Liu, C. Xie, Y. Xie, and Y. Ma, *Self-optimizing machine learning potential assisted automated workflow for highly efficient complex systems material design* (2025), arXiv:2505.08159 [cond-mat.mtrl-sci].